11-2005

A Three-Dimensional Reconstruction Algorithm for an Inverse-Geometry Volumetric CT System

Taly Gilat Schmidt
Marquette University, tal.gilat-schmidt@marquette.edu

Rebecca Fahrig
Stanford University

Norbert J. Pelc
Stanford University

Medical Physics, Vol. 32, No. 11 (November 2005): 3234-3245. DOI.

A Three-dimensional Reconstruction Algorithm for an Inverse-geometry Volumetric CT System

Taly Gilat Schmidt
Department of Radiology, Stanford University, Stanford, California
Department of Electrical Engineering, Stanford University
Rebecca Fahrig
Department of Radiology, Stanford University, Stanford, California
Norbert J. Pelc
Department of Radiology, Stanford University, Stanford, California
Department of Bioengineering, Stanford University

Abstract

An inverse-geometry volumetric computed tomography (IGCT) system has been proposed capable of rapidly acquiring sufficient data to reconstruct a thick volume in one circular scan. The system uses a large-area scanned

source opposite a smaller detector. The source and detector have the same extent in the axial, or slice, direction, thus providing sufficient volumetric sampling and avoiding cone-beam artifacts. This paper describes a reconstruction algorithm for the IGCT system. The algorithm first rebins the acquired data into two-dimensional (2D) parallel-ray projections at multiple tilt and azimuthal angles, followed by a 3D filtered backprojection. The rebinning step is performed by gridding the data onto a Cartesian grid in a 4D projection space. We present a new method for correcting the gridding error caused by the finite and asymmetric sampling in the neighborhood of each output grid point in the projection space. The reconstruction algorithm was implemented and tested on simulated IGCT data. Results show that the gridding correction reduces the gridding errors to below one Hounsfield unit. With this correction, the reconstruction algorithm does not introduce significant artifacts or blurring when compared to images reconstructed from simulated 2D parallel-ray projections. We also present an investigation of the noise behavior of the method which verifies that the proposed reconstruction algorithm utilizes cross-plane rays as efficiently as in-plane rays and can provide noise comparable to an in-plane parallel-ray geometry for the same number of photons. Simulations of a resolution test pattern and the modulation transfer function demonstrate that the IGCT system, using the proposed algorithm, is capable of 0.4 mm isotropic resolution. The successful implementation of the reconstruction algorithm is an important step in establishing feasibility of the IGCT system.

I. INTRODUCTION

Conventional computed tomography (CT) systems are rapidly evolving to acquire increasingly thicker volumes per circular rotation using multirow detectors or flat panel digital detector technology. These volume CT approaches provide several advantages over single slice acquisition, including faster scan times, thinner slices, and reduced motion artifacts. The ability to scan an entire organ in one rotation could have important clinical impact, for example, in perfusion studies and other dynamic applications.

The increased volume thickness comes at the expense of larger cone-beam angles. Because of the diverging x-ray beam in the axial, or slice, direction, a circular scan cone-beam acquisition does not acquire sufficient volumetric data.[1] Although approximate reconstruction algorithms are commonly used,[2] the resulting artifacts can be significant for large cone-angles. While exact reconstruction is possible for helical cone-beam scanning for certain pitch values,[3–6] this paper focuses on sufficient volumetric acquisition in one circular scan.

We have previously proposed a volumetric CT system that can sufficiently sample a thick (on the order of several centimeters) volume in one fast circular scan.[7] This inverse-geometry volumetric CT system (IGCT) uses a large-area scanned source and an area detector with a smaller extent in the transverse direction. The sampling is fanlike in the transverse direction, and in the axial direction the source and detector have the same extent, providing sufficient volumetric coverage and avoiding cone-beam artifacts. In addition, the smaller detector area may provide significant advantages over conventional cone-beam systems with respect to cost and detected scatter radiation.

Previous work studied the feasibility of the IGCT system with respect to sampling and photon flux and found it possible to sample a 30-cm wide field of view (FOV) with 15-cm volume thickness in less than half of a second.[7] In fact, the source scanning is sufficiently fast so that the scan time is limited by gantry speed rather than sampling. Another important feasibility question is whether the acquired IGCT data can be reconstructed accurately (from an artifact perspective) and efficiently (from a noise perspective). The purpose of this paper is to present a reconstruction algorithm for the IGCT system.

The data acquired by the IGCT geometry are very similar to that from a multiring positron emission tomography (PET) geometry. Therefore a PET reconstruction algorithm can be used. As in a three-dimensional (3D) PET system, the IGCT data consists of in-plane rays which connect each source row to the opposed detector row, and

cross-plane rays which connect each source row to other detector rows. It is the in-plane rays that ensure a sufficient dataset for accurate volumetric reconstruction, while the cross-plane rays improve the signal-to-noise ratio (SNR).

Numerous algorithms have been proposed for 3D PET. One class of algorithms uses 3D filtered backprojection.[8–10] The data are rebinned into 2D parallel-ray projections at multiple tilt and view angles, and the central slice theorem is used to derive appropriate filters in frequency space. The filtered projections are then backprojected into the volume. The IGCT reconstruction algorithm proposed in this paper follows this 3D filtered backprojection approach. Although this type of algorithm has been thoroughly studied for PET imaging, the application to a CT system merits additional research. CT produces images of higher spatial resolution and lower noise than PET and therefore demands more accurate reconstruction. Further, the process by which IGCT data are converted for use by this type of algorithm has not been explored.

The paper begins with a brief description of the IGCT system, followed by an overview of the theoretical foundation of the reconstruction algorithm. The key difference between the IGCT and 3D PET geometries is the ray sampling, which is accounted for during rebinning. Once the data are organized into 2D parallel-ray projections, the geometry is equivalent to that of 3D PET after rebinning and the already established filters can be used. Therefore, we focus much of our investigation on the rebinning algorithm and only briefly review the filter design. Gridding is used to rebin the data. We show that errors can arise due to the location of acquired data samples relative to the output grid point, and we present a new method for reducing this gridding error. The paper then investigates the image artifact, resolution, and noise performance of the algorithm through simulations. Finally, alternative reconstruction methods are briefly discussed.

II. SYSTEM DESCRIPTION

The basic system geometry is illustrated in Fig. **1**. The IGCT system consists of a large-area scanned x-ray source mounted on a CT gantry opposite a smaller array of fast photon-counting detectors. During an acquisition, the electron beam is electromagnetically steered over a transmission target, dwelling behind each of an array of collimator holes which limit the resulting x rays to those that illuminate the detector area. For each source position, the entire detector array is read out, creating a 2D divergent projection of a fraction of the field of view. The scanning of the source positions is fast relative to the gantry rotation.

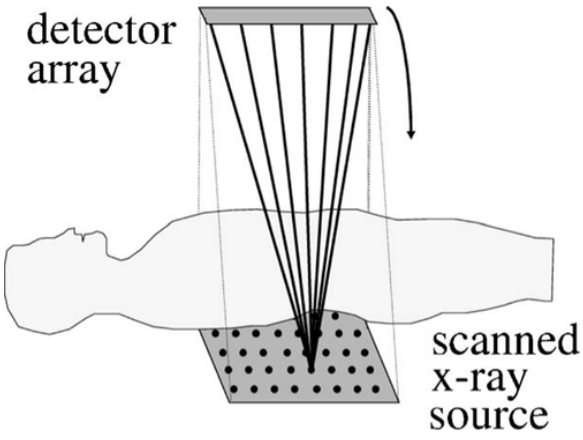

Figure 1 Proposed IGCT geometry shown with the x-ray beam at one position in the source array.

III. RECONSTRUCTION ALGORITHM

III.A. Rebinning

The goal of the rebinning algorithm is to estimate, from the rays in the IGCT geometry, a full set of 2D parallel-ray projections. The parallel-ray geometry is illustrated in Fig. **2**. We define the axis of rotation to be along the z axis, and axial planes to be perpendicular to the axis of rotation. We assume that a parallel-ray projection is formed by the set of rays normal to a virtual planar detector. The rotation of the projection about the axis of rotation (i.e., view angle), is defined as δ, while the rotation from the axis of rotation (i.e., colatitude or tilt angle) is defined as ϑ. Parameters *u* and *v* represent the local coordinates within each projection (i.e., where a ray falls on the detector). For all projections, the *u* axis lies within an axial plane.

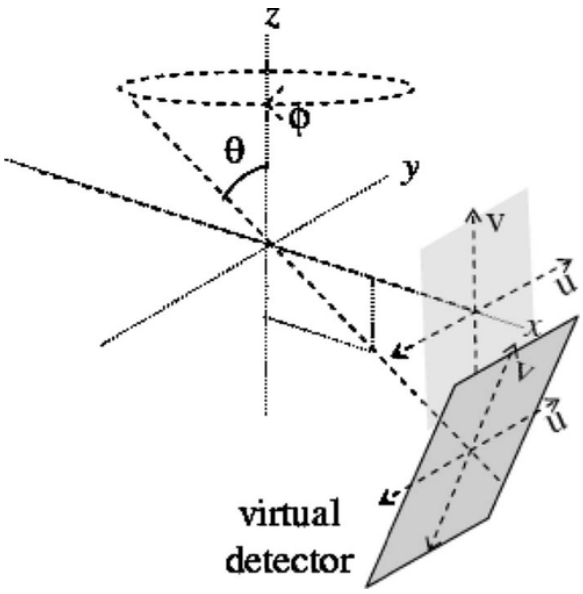

Figure 2 2D parallel-ray geometry to which the IGCT data is rebinned is illustrated using a virtual detector. ϕ is the projection view angle, θ is the colatitude angle, and *u* and *v* are the coordinates within the projection. For comparison, two virtual detectors are shown, one with θ equal to π / 2 and one with a smaller value of θ.

These four parameters, ϕ, θ, u, and v, can be calculated for each ray in the IGCT geometry. We define ψ, to be the azimuthal angle of a ray, (i.e., the angle about the z axis in the absence of gantry rotation). The parameters are illustrated in the context of the IGCT geometry in Fig. 3. A ray with ϕ equal to zero and θ equal to π / 2 is parallel to the x axis, and a ray with θ equal to zero is parallel to the z axis.

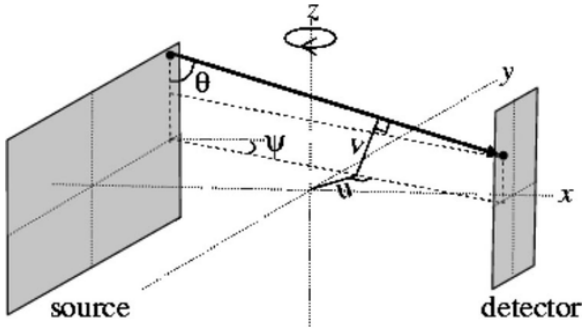

Figure 3 Four geometry parameters, ψ, θ, u, and v, shown for a ray in the IGCT geometry where ψ is the azimuthal angle.

The parameters depend on the 3D locations of the source and detector element that define the ray and can be calculated using the following equations. The coordinates (S_x, S_y, S_z) define the location of the source spot before gantry rotation, where $-S_x$ is the source-to-isocenter distance (SID). Similarly, each detector has coordinates (d_x, d_y, d_z) before gantry rotation, where d_x is the detector-to-isocenter distance (DID). Parameters ψ, θ, u, and v are independent of the gantry rotation and are calculated using the coordinates of the unrotated source and detector. Parameters ψ and u can be calculated by considering the projection of the ray onto the $x - y$ plane.

$$\psi = \arctan\left(\frac{s_y - d_y}{d_x - s_x}\right),$$

(1)

$$u = d_y \cdot \cos(\psi) + d_x \cdot \sin(\psi).$$

(2)

The total view angle φ depends both on ψ and the gantry rotation angle ϕ gantry.

$$\varphi \ = \ \psi \ + \varphi\text{gantry}.$$

(3)

The parameters θ and v can be calculated by considering the plane defined by the ray and the source column from which the ray originates.

$$\theta = \frac{\pi}{2} - \arctan\left(\frac{s_z - d_z}{\sqrt{(s_x - d_x)^2 + \left(s_y - d_y\right)^2}}\right),$$

(4)

$$v = d_z \cdot \sin(\theta) + \left[d_x \cdot \cos(\psi) - d_y \cdot \sin(\psi)\right]\cos(\theta).$$

(5)

In this formulation, the distance of the ray to isocenter is parametrized by the two perpendicular components u and v, which are equivalent to the parallel-ray detector coordinates shown in Fig. 2.

The four parameters, ϕ, θ, u, and v, are sufficient for reorganizing the IGCT data into 2D parallel-ray projections. However, for a discrete implementation with regularly sampled output 2D projections that are equally spaced in the two angles, some form of interpolation must be used.

In order to better understand the rebinning algorithm, it is helpful to visualize the data in projection space. For a 2D reconstruction from 1D projections, such as those acquired by conventional single slice CT systems, each ray is described by two parameters, the rotation angle ϕ and the radial distance to isocenter ρ. For these single slice CT systems, projection space is two dimensional with coordinate axes ρ and ϕ. Each ray in a 1D projection samples one point in the two-dimensional projection space, and a 1D parallel-ray projection, comprised of data at one ϕ value and a range of ρ values spanning the field of view, samples a horizontal line in projection space.

In the IGCT geometry, each ray is described by two angles and two distances and is represented in a 4D projection space. Each ray samples one point in the 4D projection space, but the sample points from all acquired

rays are not uniformly distributed. Rebinning the data to 2D parallel-ray projections is equivalent to interpolating the nonuniform samples onto a 4D Cartesian grid in projection space. The problem of resampling nonuniform data onto a uniform grid arises in many different fields and has been the subject of much work. We are using a gridding approach[11] in which each acquired data point contributes to all output grid points within some neighborhood. In this implementation, a bin width is selected for each of the four projection space parameters, defining the 4D neighborhood of measured data points used to estimate each grid point. Each data point in this bin is weighted based on its 4D location with respect to the grid point and a chosen 4D kernel shape. The interpolated value at the grid point is the sum of the weighted data points, normalized by the sum of weights for that point.

The important design parameters for the rebinning algorithm are the bin widths, kernel shape, and output grid sampling density. For application in magnetic resonance (MR) reconstruction, the effect of each of these parameters on the gridded data has been described in detail.[12] Although most medical imaging applications, including MR, apply gridding in frequency space, the analysis in Ref. **12** is based on general signal processing theory and is relevant for other applications. When gridding in projection space, special care must be taken to properly combine rays that are physically close yet separated in angle. For example, rays near $\phi = 2\pi$ must be considered when gridding data at $\phi = 0$.

III.B. Rebinning error correction

One important step in the gridding algorithm is compensation for the nonuniform and/or asymmetric location of the acquired data points. That is, the estimated grid point value should not be biased by the number or the distribution of measured data points used in the estimation. Errors can occur if the sampling is not accounted for properly.

The simplest method for performing this correction is post-compensation, where the value at the output grid point is normalized by the total sum of the deposited weights. After this normalization, and considering gridding of a 1D function $f(x)$, the gridded value at a point x_o is

$$\hat{f}(x_o) = \sum ik_i f(x_i),$$

(6)

where $f(x_i)$ is the ith input sample and k_i is the normalized kernel value for that sample. This method corrects for the number of data points that contribute to a grid point and gives an unbiased estimate if the data are locally constant. That is, if $f(x_i) = f(x_o)$ for all i, Eq. (6) gives the correct answer since the sum of the k_i is one. However, consider the particular but relatively simple case where the input function is linear with slope G.

$$f(x) = f(x_o) + G(x - x_o).$$

(7)

Straight-forward gridding yields

$$\hat{f}(x_o) = \sum_i k_i[f(x_o) + G(x_i - x_o)],$$

(8)

which reduces to

$$\hat{f}(x_o) = f(x_o) + G\sum_i k_i(x_i - x_o).$$

(9)

Since the desired value is $f(x_o)$, the second term on the right-hand side of Eq. (9) is the gridding error ϵ.

$$\epsilon = G \sum_i k_i (x_i - x_o).$$

(10)

If the kernel is even and the samples are symmetric about x_o, the error is zero. In general, though, there is an error proportional to the slope of the input function. In our implementation, we are gridding the projection measurement data. Therefore, it is the gradient of the projection of the object that determines the amount of error in the gridded value.

In addition, we have found that the error caused by the linear term and the asymmetric sampling can be coherent in adjacent gridded projection angles, causing an artifact to accumulate in the image. This can be understood by considering the distribution of data points about a particular grid point. If the data points are asymmetrically distributed in the radial direction, the interpolated value at the grid point will be biased in the direction with more samples. For example, if the projection measurements are higher on the side with more samples, the gridding output may overestimate the correct value. The asymmetric sampling will likely bias a grid point at a nearby radial location in the opposite direction (note that the gain of the gridding process is unity). In our system, each view samples data from a range of azimuthal and radial positions. The radial sampling varies slowly with azimuthal angle within each IGCT view, and repeats for each gantry position. Since the overall trends of projections also vary slowly with view angle, rebinned projections at nearby azimuthal angles will contain similar errors. In other words, the gridding error will vary rapidly in the radial direction and slowly in the azimuthal direction, which is the type of error to which CT is particularly sensitive.

A more sophisticated gridding approach preweights the data by the inverse sampling density of the measurements. That is, data from highly sampled regions are deemphasized while data from sparsely sampled regions are emphasized by the preweighting factors. For certain sampling patterns, such as spiral sampling in MR, these density weights can be calculated analytically.[13] Several other approaches, including computational and iterative methods, have been proposed to determine the weights for arbitrary sampling patterns.[14–16] While preweighting should reduce errors, we note that Eq. **(10)** predicts residual errors even with uniform sampling density.

The uniform resampling algorithm (URS), which is optimal in the minimum norm least square sense, and the block uniform resampling algorithm (BURS), a computationally feasible locally optimal gridding algorithm, have also been proposed.[17] These algorithms indirectly incorporate the sampling pattern when estimating the grid points by formulating the gridding problem as a linear set of equations and using least-squares methods to solve for the values at the grid points. These methods are sometimes ill-conditioned and may be sensitive to noise or measurement errors. A regularized version has also been proposed which provides stability at the expense of accuracy.[18]

Most of the methods listed above were developed for gridding in frequency space and are largely applied to MR imaging. Gridding in projection space has slightly different challenges.[19] Due to the ramp filter in CT reconstruction, errors that are high in frequency in the radial direction are greatly amplified. Also, the dynamic range (the range of reconstructed values divided by the noise level) of CT demands a higher signal-to-artifact level compared to MR or PET. For example, CT is sensitive to errors on the order of a few Hounsfield units (HU), where one HU is a change in signal that is one tenth of one percent of the attenuation of water, while the range of values may be 400% of the density of water.

Therefore, we propose a new gridding correction that is motivated by Eq. (10). We note that if the sum in the error term was zero, the grid point value would be correct (for this case) regardless of the slope. We modify each kernel value k_i by an amount which depends on the distance between the data point and grid point. We define the new kernel values, k_{new_i} as

$$k\_new_i = k_i + \delta(x_i - x_o),$$

(11)

and solve for the value of δ such that the sum in Eq. (10), and therefore the error, equals zero.

$$0 = \sum_i [k_i + \delta(x_i - x_o)](x_i - x_o)$$

(12)

$$\delta = \frac{-\sum_i k_i(x_i - x_o)}{\sum_i (x_i - x_o)^2}.$$

(13)

By using the kernel values defined in Eqs. **(11)** and **(13)**, the zero and first-order terms of the projection data are estimated correctly at the grid points. This local kernel correction strategy can be generalized to ensure that higher-order terms are correctly estimated, but since we only use the data in a small neighborhood about each grid point, the higher-order terms should be small. In addition, the higher-order terms are less likely to be similar in neighboring projections and should not lead to the coherent errors.

Although the proposed correction does not explicitly compute the measurement sampling density, the modified kernel values in Eq. **(11)** can be thought of as compensating for this as well as resymmetrizing the kernel based on the distribution of data points. A post-compensation step to ensure that the total sum of weights at each grid point is one is still required. The gridding correction can produce negative kernel values which may cause the sum of the kernel values at the grid point to be very small. This occurs when the measured data points are clustered close together on one side of the grid point. When the kernel value sum is very small, the post-compensation step amplifies the contribution of some data points and the noise. Therefore, a threshold is set on the sum of the corrected kernel values. If the sum is below the threshold, the original kernel values are used.

This method can be easily extended to multiple dimensions. In the case of 2D gridding, the locally linear function is

$$f(x, y) = f(x_o, y_o) + \frac{\partial f}{\partial x} f(x - x_o) + \frac{\partial f}{\partial y} f(y - y_o).$$

(14)

The grid point value at (x_o, y_o) estimated from data points at (x_i, y_i) is

$$f(x_o, y_o) = \sum_i k_i f(x_i - y_i),$$

(15)

and the adjusted kernel values are defined by

$$k\_new_i = k_i + \delta_x(x_i - x_o) + \delta_y(y_i - y_o),$$

(16)

where δ_x and δ_y are determined by solving the following equations:

$$\begin{aligned}\delta_x \sum_i (x_i - x_o)^2 + \delta_y \sum_i (x_i - x_o)(y_i - y_o) \\ = -\sum k_i (x_i - x_o) \delta_y \sum_i (y_i - y_o)^2 + \delta_x \sum_i (x_i - x_o)(y_i - y_o) \\ = -\sum k_i (y_i - y_o).\end{aligned}$$

(17)

The solution in Eq. **(17)** is not well-defined when the system of equations is ill-conditioned. This could be the case in sparsely sampled regions where there is an insufficient distribution of data points surrounding a grid point. This will cause the calculated δ values to be very large, which may lead to unstable performance. A threshold on the allowed size of δ can be set, and for grid points for which this threshold is exceeded, either the original kernel values can be used, or the region size used to estimate the grid point can be expanded.

For our geometry, the gridding correction is applied in four dimensions, which requires solving a system of four equations to ensure that the linear term is correctly estimated.

III.C. Filtered backprojection

Once the data are organized into 2D parallel-ray projections, the central slice theorem can be used to design the appropriate reconstruction filter. The theorem states that a 2D parallel-ray projection of a 3D object samples the 3D Fourier transform of the object along the plane that is perpendicular to the projection direction and that passes through the origin. Therefore the ensemble of parallel-ray projections sample the Fourier transform of the object, with some areas of frequency space sampled more than others.

The role of the reconstruction filters is to weight the frequency content of each projection so that, when they are all superimposed during backprojection, the 3D Fourier transform of the object is properly reconstructed. One solution is to define the filter applied to each projection to be the inverse of the density of measurements in frequency space on the plane sampled by that projection.

An analytical expression for this filter, known as the "Colsher" filter, has been previously derived[8,10] and is stated without proof below. The derivation assumes 2D parallel-ray projections continuously and uniformly distributed between ϕ equal to zero and 2π and colatitude angle between $\theta_{\min}$ and $\pi/2$, where $\theta_{\min}$ is the colatitude angle of the most oblique projection. These assumptions are reasonable if the distance between adjacent projections is small in both angular directions. The density of measurements, stated without proof, is

$$D_\theta(k, \alpha) = \frac{M \arcsin\left[\frac{\cos(\theta')}{\sin(\alpha)}\right]}{\pi k \cos(\theta_{\min})},$$

(18)

$$k = \sqrt{k_u^2 + k_v^2},$$

(19)

$$\alpha = \arccos\left(\frac{k_v \sin\theta}{k}\right),$$

(20)

$$\theta' = \max\left(\theta_{\min}, \frac{\pi}{2} - \alpha\right),$$

(21)

where k_u and k_v are the coordinates of the 2D Fourier transform of the projection and M is the total number of projections.

The 2D filter for a parallel-ray projection at a colatitude angle θ is then given by

$$G_\theta(k_u, k_v) = \frac{W(k)}{D_\theta(k, \alpha)},$$

(22)

where $W(k)$ is a window function used to control the impulse response. Substituting the expression for D_θ the resulting 2D filter is

$$G_\theta(k_u, k_v) = \frac{\pi k \cos(\theta_{\min})}{M \arcsin\left(\frac{\cos(\theta')}{\sin(\alpha)}\right)} W(k).$$

(23)

As can be seen in Eq. (23), the filter depends on the colatitude angle θ but is the same for all view angles at that θ.

The window function $W(k)$ can be designed to recover some of the resolution lost during the rebinning step. The gridding algorithm convolves the input data with a 4D kernel causing some apodization in frequency space. During the filtering step, the Fourier transform is performed in two spatial dimensions, u and v. Therefore, in these two dimensions, the blurring due to gridding can be undone by incorporating into the filter window the inverse of the Fourier transform of the gridding kernel. The blurring in the two angular dimensions cannot be reduced during the normal filtering step but could be deapodized in a separate step prior to backprojection.

The filter in Eq. **(23)** is defined as a continuous function in frequency space. Implementing the filter discretely can introduce low frequency artifacts in the reconstructed image due to aliasing of the filter in image space.[20] To reduce these artifacts, the discrete filters are first oversampled in frequency space, windowed in image space, and then transformed back to frequency space.[21] In this way the filter for each colatitude angle is calculated as part of the preparation for image reconstruction. During reconstruction, each 2D parallel-ray projection is filtered with the 2D filter for the appropriate θ and backprojected into the 3D volume. We used a pixel-driven backprojection with linear interpolation.

III.D. Projection truncation

Due to the finite longitudinal extent of the source and detector, oblique rays do not encompass the entire field of view, as illustrated in Fig. **4**. Depending on the size of the object, the rebinned 2D parallel-ray projections at these oblique colatitude angles will be truncated and cannot be directly incorporated into the filtered backprojection algorithm. One known method for dealing with these truncated projections performs an initial reconstruction from the complete projections at $\theta = \pi/2$ and then uses reprojection to estimate the missing rays.[22] The completed set of projections can then be used to reconstruct the 3D volume using the method described above.

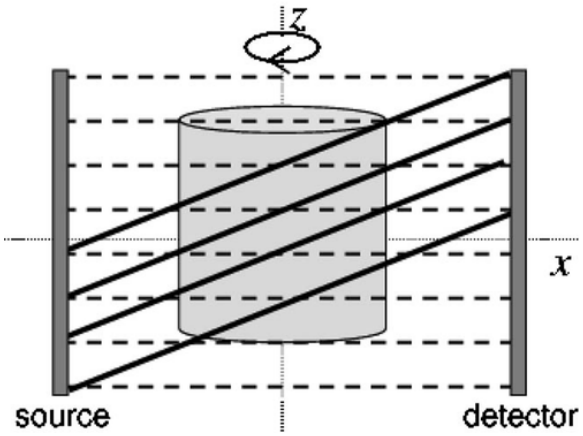

Figure 4 Profile of the source and detector illustrates that while the in-plane rays span the entire longitudinal field of view, cross-plane rays at oblique colatitude angles do not cover the entire object, leading to truncated parallel-ray projections.

For the preliminary investigation of this algorithm, the reprojection algorithm was not implemented. Instead, the longitudinal FOV was reduced somewhat and only projections at colatitude angles that contain the entire object were used to reconstruct the volume. Although this simplification inefficiently uses the collected data and would suffer a large SNR penalty in a real system, it is acceptable for the preliminary investigation of the integrity of the algorithm in the absence of noise. When studying the noise performance of the algorithm, projections from all colatitude angles were used as will be described in Sec. **IV D**.

III.E. Noise considerations

The IGCT geometry contains cross-plane ray measurements, and in order to provide suitable noise performance, the reconstruction algorithm must use these rays efficiently, ideally as efficiently as the in-plane rays. To study this requirement we use the metric of photon utilization efficiency. We distribute the same total number of photons to the IGCT system and to a parallel-ray geometry that uses only in-plane rays, where both systems have comparable resolution and field of view, and compare the noise in the resulting images.

The noise in a reconstructed CT voxel depends on the spatial resolution and the number of photons that passed through the voxel and were detected as expressed in the following equation:[23]

$$\sigma^2 = A \cdot \sum_{j=1}^{m} \frac{1}{N_j},$$

(24)

whereN_j is the mean detected photon density that has passed through the voxel in the jth projection, m is the number of projections, and A is the integral of the reconstruction filter squared. For parallel-ray reconstruction using only in-plane rays, A can be expressed as

$$A = \frac{\pi^2}{m^2} \int_{-\infty}^{\infty} \int_{-\infty}^{\infty} k_u^2 \, |W(k_u, k_v)|^2 dk_u dk_v,$$

(25)

where k_u and k_v are the coordinates of the 2D Fourier transform of the projection, and W is the window function, in our case a radial Hanning window with frequency cutoff k_c,

$$W(k_u, k_v) = \frac{1}{2}\left[1 + \cos\left(\frac{\pi\sqrt{k_u^2 + k_v^2}}{k_c}\right)\right] \sqcap \left(\frac{\sqrt{k_u^2 + k_v^2}}{2k_c}\right).$$

(26)

By combining Eqs. (24), (25), and (26), and assuming that the photon density N is the same for all projections, we can calculate the photon density required to achieve a specified noise variance.

$$N = \frac{\pi^2 \int_{-\infty}^{\infty} \int_{-\infty}^{\infty} k_u^2 \left|W\left(k_u^2, k_v^2\right)\right|^2 dk_u dk_v}{m\sigma^2}.$$

(27)

From the photon density, which is defined as the number of photons per unit area, the total number of photons in the parallel-ray acquisition is

$$P_{\text{total}} = N \cdot pix_u \cdot pix_v \cdot area_d \cdot m,$$

(28)

wherepix_u and pix_v are the detector dimensions in pixels, and $area_d$ is the area of a detector element.

By distributing P_{total} photons to the IGCT geometry and measuring the resulting noise, we can compare the IGCT photon utilization efficiency to that of the in-plane parallel-ray geometry. That is, we can examine whether the proposed reconstruction algorithm uses the cross-plane rays as effectively as the in-plane rays.

IV. SIMULATIONS

To test the reconstruction algorithm, projection data were simulated for the IGCT geometry. The specifications of the simulated system are summarized in Table **I** and are based on hardware components developed by NexRay Inc. (Los Gatos, CA),[24] but with SID and DID typical of a CT geometry (but reversed). At each gantry position data are collected from each of the 2000 source spots. We assumed the acquisition of these data was instantaneous, i.e., no rotation during source scanning. Sixty-three gantry positions over 2π were determined necessary for sufficient sampling (note that each view contributes to many 2D projections).[7] The source and detector apertures were simulated by averaging data from discrete subsources and subdetectors spanning the finite aperture sizes.

Table I. Simulated IGCT geometry.

Source dimensions (transverse × axial)	25×5 cm
Number of source locations (transverse × axial)	100×20
Detector dimensions (transverse × axial)	5.4×5.4 cm
Number of detector elements (transverse × axial)	48×48
SID	41 cm
DID	54 cm
FOV (transverse × axial)	12×5 cm
Number of views over 2π	63
Source focal spot width	0.06 cm
Detector aperture width	0.11 cm

The data were rebinned into a 2D parallel-ray geometry using the parameters specified in Table **II**. While a thorough optimization was not performed, the gridding parameters were selected experimentally to provide acceptable performance. The projection sampling was chosen to be $0.125\ \text{mm} \times 0.125\ \text{mm}$, as using an oversampled grid improves the gridding performance.[12] For computational convenience, the number of rebinned views was 1008, which is 16 times the number of acquired views. By using this number of rebinned views, the distribution of measurements in the 4D projection space repeats for every 16 grid points in the ϕ direction. The precorrection kernel weights were based on a separable 4D Hanning window. The implemented kernel widths provided a reasonable tradeoff between the resulting blur and having sufficient measurements to estimate each grid point. Further, the selected kernel widths were large enough to ensure that all data points were used. The threshold on the sum of the kernel values was initially set to zero and was then increased until the related artifacts were qualitatively absent from the rebinned projections. The maximum δ value was chosen by examining a histogram of all calculated δ values and choosing a reasonable threshold.

Table II. Rebinning algorithm parameters.

2D projection sampling	$0.0125 \times 0.0125\ \text{cm}$
2D projection dimensions	352×960 pixels
Number of views over 2π	1008
Maximum colatitude angle	$\pi/2\ \text{rad}$
Minimum colatitude angle	$\pi/2 - 0.03\ \text{rad}$
Colatitude angle spacing	$0.003\ \text{rad}$
Radial kernel width (u, v)	$0.07\ \text{cm}$
Angular kernel width (φ, θ)	$0.0126\ \text{rad}$
Minimum sum of corrected kernel values	0.6
Maximum δ value	1000

The reconstruction filter was apodized with a Hanning window with a cutoff of $15\ \text{lp/cm}$ unless otherwise noted. For the rebinned IGCT data, the projections were further windowed with the inverse of the Fourier transform of the gridding kernel, as discussed in Sec. **III C**, unless otherwise stated.

IV.A. Water sphere

To measure the artifact level in the reconstructed volume, data from the IGCT system and a comparable 2D parallel-ray geometry were simulated through a water sphere located at $(1\ \text{cm},\ 1\ \text{cm},\ 0\ \text{cm})$ with a radius of $2\ \text{cm}$.

IV.B. MTF

A $0.006\ 25\ \text{cm}$ radius sphere at isocenter was simulated in order to investigate the resolution effects of the reconstruction algorithm. The IGCT source focal spot and detector aperture were modeled as part of the simulation. The modulation transfer function (MTF) was calculated by reconstructing a volume containing the sphere, projecting the volume perpendicularly to the axis of rotation, and computing the 2D Fourier transform of the result. The horizontal radial line through the transform gives the MTF in the in-plane direction, while the vertical radial line gives the MTF in the slice direction. The small sphere was also simulated centered at (4, 4, $1\ \text{cm}$) to study the resolution away from the center of the field of view.

For comparison, 2D parallel-ray projections of the geometry in Table **II** were simulated for the $0.006\ 25\ \text{cm}$ sphere at isocenter. The parallel-ray data was simulated with focal spot and detector aperture blurring equivalent to the IGCT geometry so that any discrepancies in the MTF would be due to the IGCT

reconstruction algorithm. For all MTF studies, the reconstruction filter was apodized with a Hanning window with a $40\ \mathrm{lp/cm}$ cutoff.

IV.C. Resolution phantom

To further investigate the algorithm performance for high resolution objects, a phantom was simulated with 32 spheres arranged into four resolution patterns with $0.7, 0.6, 0.5$, and $0.4\ \mathrm{mm}$ spheres, respectively. For example, the $0.5\ \mathrm{mm}$ pattern contained eight $0.5\ \mathrm{mm}$ diameter spheres centered at the vertices of a $1\ \mathrm{mm}$ cube. Coronal and axial planes through the patterns were reconstructed. The cutoff of the reconstruction filter Hanning window was $40\ \mathrm{lp/cm}$.

IV.D. Noise

The photon utilization efficiency of the IGCT reconstruction was examined by using Eq. **(27)** to calculate the photon density required for an in-plane 2D parallel-ray geometry with $15\ \mathrm{lp/cm}$ bandwidth to achieve a noise standard deviation of $10\ \mathrm{HU}$. The resulting photon density, $5 \times 10^6 \mathrm{photons/cm^2}$, yields a total of $2.7\times 10^{11}\mathrm{photons}$ for the projection sampling described in Table **II**. Noisy IGCT data and in-plane parallel-ray data were simulated using this number of photons detected through air, and the central axial slice was reconstructed. The simulations were repeated five times. The full range of colatitude angles, $+/-0.3\ \mathrm{rad}$, was used in the IGCT reconstruction. Because the reprojection algorithm was not implemented, some of the projections were truncated. While the missing values were set to zero, the truncation did not significantly affect the image noise because the projections contained only noise and because only the central axial slice was reconstructed. The reconstructed noise standard deviation did not change significantly when the missing projection data was replaced by values with standard deviation equivalent to the measured rays.

V. RESULTS

V.A. Water sphere

The simulated IGCT water sphere data were first rebinned into the 2D parallel-ray geometry specified in Table **II**. Figure **5** compares a profile through an ideal parallel-ray projection and an IGCT projection rebinned with and without the gridding correction. In other words, this graph plots one line in the 4D projection space. The region highlighted in Fig. **5(a)** is expanded in Fig. **5(b)** to more clearly show the gridding errors. Figure **6** displays the difference between the parallel-ray projection and the IGCT rebinned projection with and without correction. The relationship between the gridding error before correction and the gradient of the projection is demonstrated in Fig. **6**, as the error is highest where the curve in Fig. **5(a)** is steep. The error at the edge of the object, still present in the corrected projection, is due to the blurring incurred during rebinning.

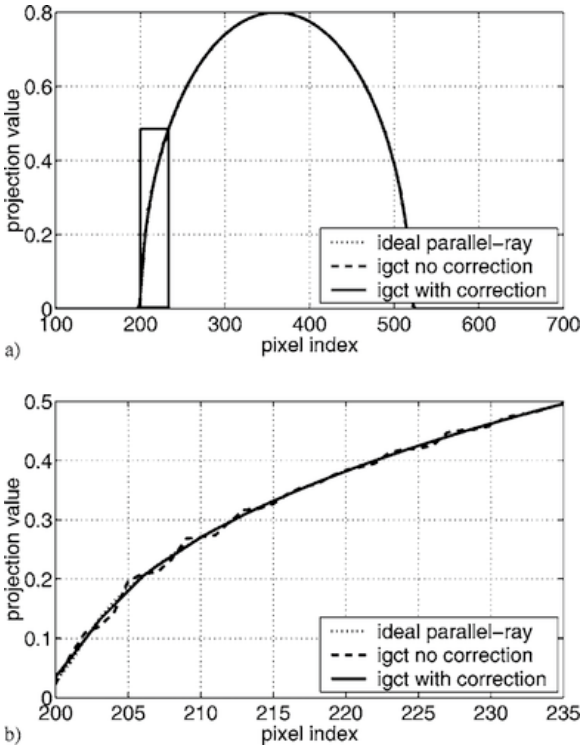

Figure 5 Profile of a water sphere projection for the ideal parallel-ray geometry and the IGCT geometry rebinned with and without the gridding correction. The highlighted region of (a) is expanded in (b).

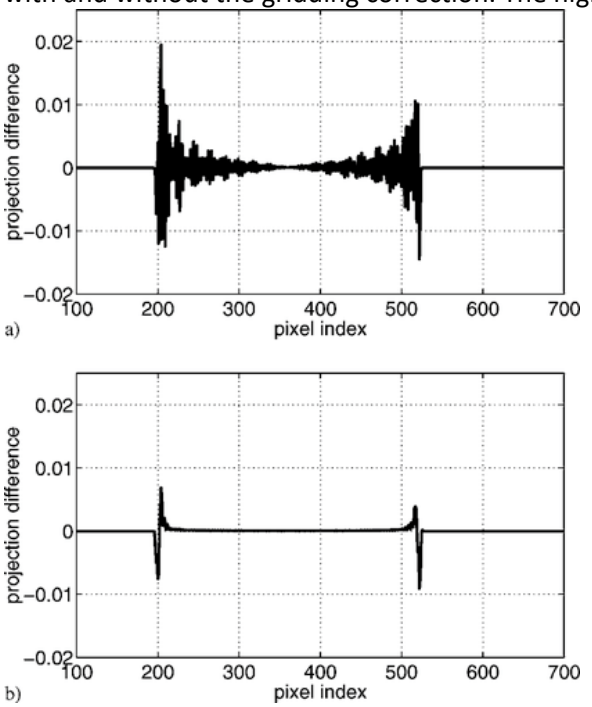

Figure 6 Difference between the parallel-ray projection and (a) the IGCT rebinned projection without gridding correction and (b) IGCT rebinned projection with correction.

The rebinned projections were then filtered and backprojected to reconstruct the central axial plane of the sphere. Figure **7(a)** shows the reconstructed plane without the gridding error correction. The image is displayed with a window centered 0 HU, and a width of $+/-1$ HU, that is pixels values below -1 HU are black, and pixel values above 1 HU are white. Figure **7(d)** plots the central horizontal profile through the image. The high

frequency gridding artifacts seen in the sphere are reduced to well below $1\ \mathrm{HU}$ by the gridding correction, as shown in Figs. **7(b)** and **7(e)**. This demonstrates that the artifacts in Fig. **7(a)** are caused by the asymmetric sampling around each output grid point, combined with the locally non-constant projection values which are relatively similar in adjacent views. With the correction up to linear terms, the IGCT reconstruction is comparable to that from direct parallel-ray data, shown in Figs. **7(c)** and **7(f)**. Although the gridding errors displayed in Fig. **7** are relatively small, on the order of $1-2\ \mathrm{HU}$, the gridding error is proportional to the gradient of the projection, and the object simulated in this experiment is by no means the worst case. Without the gridding correction, significant artifacts will result for more challenging objects.

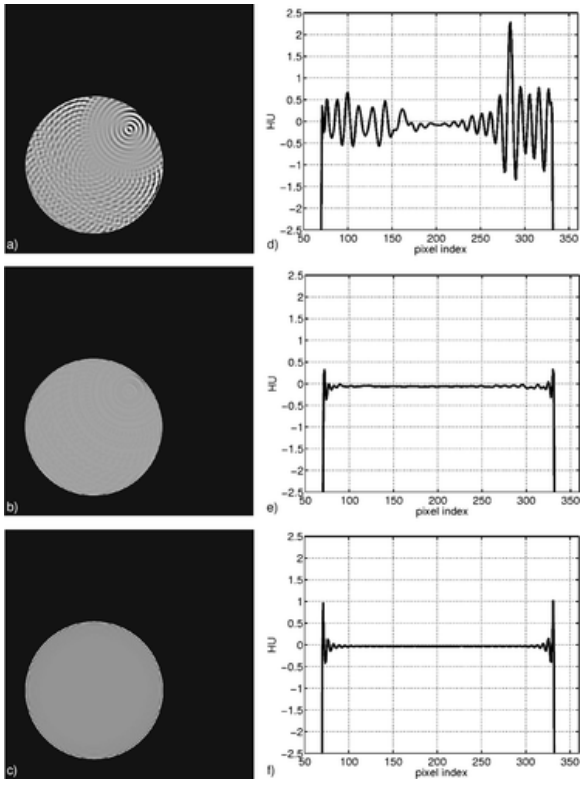

Figure 7 Reconstructed central axial plane of the off-center water sphere for (a) the IGCT simulation without gridding correction, (b) the IGCT simulation with gridding correction, and (c) the parallel-ray simulation. All images are windowed to a level of $0\ \mathrm{HU} +/-1\ \mathrm{HU}$. The central horizontal profile through the image is plotted for (d) the IGCT simulation without gridding correction, (e) the IGCT simulation with gridding correction, and (f) the parallel-ray simulation.

Figure **8** compares the central coronal plane of the sphere simulated by both the IGCT and parallel-ray geometries. The gridding correction has been applied in the IGCT reconstruction. The images are displayed at two different windows to show artifacts in both air and water, and the central horizontal profile is plotted for each reconstruction. The IGCT image contains more prominent view aliasing artifacts. However, these artifacts are small enough to be acceptable. Other than this difference, the two reconstructions have comparable image quality.

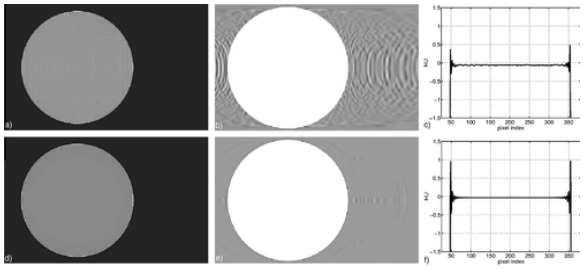

Figure 8 Reconstructed central coronal plane of the off-center water sphere for (a), (b) the IGCT simulation, and (d),(e) the parallel-ray simulation. Images (a) and (d) are windowed to $0\ \mathrm{HU} +/-1\ \mathrm{HU}$, and images (b) and (e) are windowed to $-1000\ \mathrm{HU} +/-1\ \mathrm{HU}$. The central horizontal profile through the image is shown (c) for the IGCT reconstruction and (f) for the parallel-ray reconstruction.

In the IGCT reconstruction, only rebinned parallel-ray projections containing the complete object were used. That is, only seven of the possible 21 colatitude angles were used, while the ideal parallel-ray projections were simulated at all 21 colatitude angles. Therefore the results of the IGCT simulations verify the integrity of the rebinning algorithm and the integrity of the filtered backprojection for small colatitude angles, while the results of the parallel-ray simulations verify that more oblique projections are handled properly by the filtered backprojection and do not introduce artifacts.

For efficient noise and dose performance in a real IGCT system, the reprojection algorithm would be implemented to utilize data from all colatitude angles.

V.B. MTF

The MTF was calculated for the IGCT and parallel-ray geometries, both reconstructed with a Hanning windowed reconstruction filter. IGCT reconstructions were made with and without the deapodization described in Sec. **III C** and with and without the gridding correction. Since the object is small, 21 colatitude angles were used in the IGCT simulation. Only in-plane rays were used in the direct parallel-ray simulation. Figure **9** compares the resulting MTF curves. Both the in-plane and slice MTFs are displayed for the IGCT geometry. As can be seen, while the rebinning algorithm does introduce some blurring, the resolution can be largely recovered by using the deapodization window during filtered backprojection. The slight difference between the in-plane and slice MTF is likely due to discretization errors. The 10% value of the MTF is at $16\ \mathrm{lp/cm}$. Even higher spatial resolution is possible if the Hanning window is omitted or replaced with a function with higher amplitude at high spatial frequencies. Without the Hanning window, the modulation at $16\ \mathrm{lp/cm}$ is expected to have been 15%.

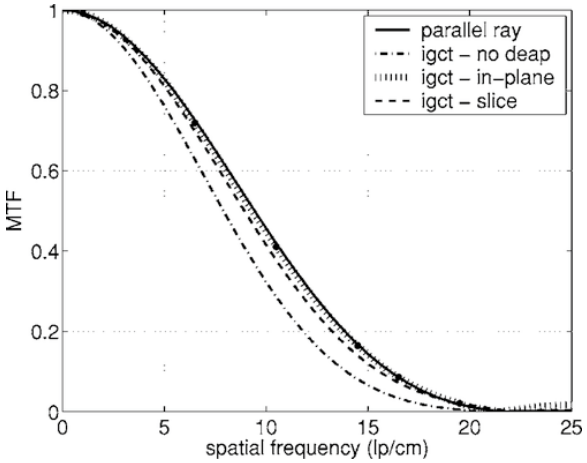

Figure 9 Plot comparing the MTF curves for the IGCT and parallel-ray simulations. The IGCT data was reconstructed both with and without the gridding kernel deapodization window. For the IGCT data with deapodization window, both in-plane and slice MTF curves are displayed.

Figure **10** compares the in-plane MTF of the IGCT system with and without the gridding error correction, verifying that the correction does not degrade the resolution.

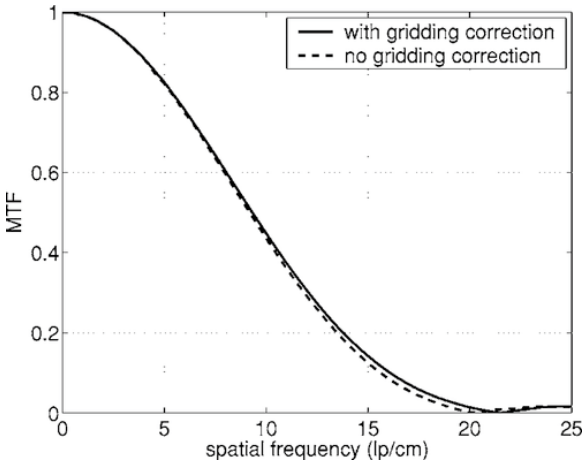

Figure 10 Comparison of the in-plane MTF curves for the IGCT system with and without the gridding correction.

Figure **11** shows the in-plane and slice MTF toward the edge of the in-plane field of view, compared to the in-plane MTF at isocenter. The slight degradation seen in the in-plane MTF is most likely due to the azimuthal blurring introduced during rebinning. If the cross-plane rays included in this reconstruction were approximated as in-plane rays, as is done in single-slice rebinning,[25] the response at the edge of the 12-cm FOV would span more than $3\ \mathrm{mm}$ in the slice direction. In the IGCT reconstruction, the slice MTF is preserved as the impulse moves off center, indicating that the gridding algorithm properly incorporates the oblique rays.

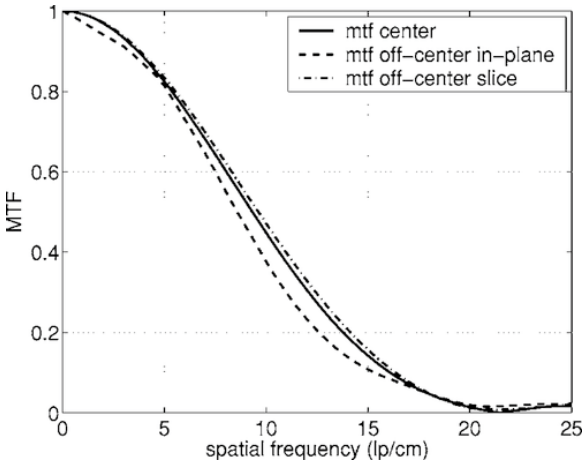

Figure 11 Comparison of the MTF curves at isocenter and toward the edge of the field of view $(4, 4,\ 1\ \mathrm{cm})$.

V.C. Resolution phantom

Figure **12** displays an axial and coronal plane through the resolution patterns, and in both images the $0.4\ \mathrm{mm}$ spheres can be resolved. Projections at all 21 colatitude angles were used in this reconstruction. The reduced modulation of the smaller sphere patterns is consistent with the MTF curve. Again, a different filter window function could be used to preserve more uniform response across all frequencies.

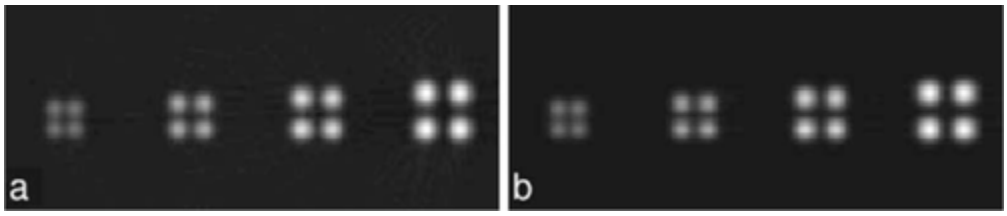

Figure 12 Reconstructed (a) axial and (b) coronal planes of the resolution phantom consisting of 0.4, 0.5, 0.6, and $0.7\ \mathrm{mm}$ resolution patterns.

V.D. Noise

Compared to the predicted $10\ \mathrm{HU}$ standard deviation, the noise standard deviation of the in-plane parallel-ray reconstructions, averaged across the five simulations, was $9.98 +/- 0.06\ \mathrm{HU}$, while the noise in the IGCT reconstruction was $7.69 +/- 0.05\ \mathrm{HU}$ before deapodization, and $9.09 +/- 0.05\ \mathrm{HU}$ after deapodization. The slightly lower noise in the IGCT images, even after apodization, may be caused by residual gridding blur. When only in-plane rays are used in the IGCT reconstruction, the resulting noise after deapodization was $19.54 +/- 0.02\ \mathrm{HU}$, thereby demonstrating the advantage of incorporating the cross-plane rays. The results of the noise investigation show that the proposed reconstruction algorithm efficiently uses the cross-plane rays and can provide noise performance similar to a comparable in-plane parallel-ray geometry when given the same number of photons.

VI. DISCUSSION AND CONCLUSIONS

The results presented in this paper demonstrate acceptable performance of the 3D filtered backprojection algorithm proposed for the IGCT geometry. This reconstruction method is one of several possible approaches for the IGCT data. One alternative is Fourier rebinning (FORE).[26,27] These algorithms estimate the in-plane data from the cross-plane data, thereby requiring only a 2D filtered backprojection. Another advantage of these methods is that they avoid the data truncation problem and do not require the time consuming reprojection step. The FORE algorithm has been applied to PET data with much success.[26–31] An exact Fourier rebinning algorithm, FORE-J, which also avoids the reprojection step has been proposed.[27] These Fourier rebinning algorithms are very promising and their implementation for the IGCT geometry would be interesting future work, as would the investigation of iterative reconstruction algorithms.

Our work shows that the use of a gridding method can introduce errors when the sampling pattern surrounding each output point is asymmetric and that these errors are significant in rebinning for CT reconstruction. We developed a correction method that effectively reduces the errors associated with gridding. We believe this method is new and that it may be useful in other applications such as non-Cartesian MR imaging. With this correction, we demonstrated that high quality images, relatively free of artifacts and additional blurring, can be produced from IGCT data. The noise investigation demonstrates that the proposed reconstruction algorithm uses the cross-plane rays as efficiently as the in-plane rays and provides noise comparable to an in-plane parallel-ray geometry when both systems use the same number of photons. The simulations presented in this paper further predict that an isotropic resolution of $0.4\ \mathrm{mm}$ can be achieved using realizable source and detector components and the proposed algorithm. Although much work remains to fully investigate the feasibility of the IGCT system, the encouraging performance of the reconstruction algorithm further supports the potential for high quality volumetric scanning free from cone-beam artifacts using the IGCT geometry.

ACKNOWLEDGMENTS

This work is supported by GE Healthcare. The authors would like to thank Ed Solomon and Josh Star-Lack of NexRay, Inc. and Robert Bennett of Stanford University for helpful discussions.

REFERENCES

1 B. D. Smith, " Cone-beam tomography: recent advances and a tutorial review," *Neuropsychobiology* **29**, 524– 534 (1990).

2 L. A. Feldkamp, L. C. Davis, and J. W. Kress, " Practical cone-beam algorithm," *J. Opt. Soc. Am. A* **1**, 612– 619 (1984).

3 A. Katsevich, " Theoretically exact filtered backprojection-type inversion algorithm for spiral CT," *SIAM J. Appl. Math.* 10.1137/S0036139901387186 **62**, 2012– 2026 (2002).

4 A. Katsevich, " Analysis of an exact inversion algorithm for spiral cone-beam CT," *Phys. Med. Biol.* 10.1088/0031-9155/47/15/302 **47**, 2583– 2598 (2002).

5 A. Katsevich, " A general scheme for constructing inversion algorithms for cone beam CT," *Int. J. Math. Math. Sci.* 10.1155/S0161171203209315 **21**, 1305– 1321 (2003).

6 G. H. Chen, " An alternative derivation of Katsevich's cone-beam reconstruction formula," *Med. Phys.* 10.1118/1.1628413 **30**(12), 3217– 3216 (2003).

7 T. G. Schmidt, R. Fahrig, E. G. Solomon, and N. J. Pelc, " An inverse-geometry volumetric CT system with a large-area scanned source: A feasibility study," *Med. Phys.* 10.1118/1.1786171 **31**(9), 2623– 2627 (2004).

8 J. G. Colsher, " Fully three-dimensional positron emission tomography," *Phys. Med. Biol.* **25**(1), 103– 115 (1979).

9 M. Defrise, D. W. Townsend, and R. Clack, " Three-dimensional image reconstruction from complete projections," *Phys. Med. Biol.* 10.1088/0031-9155/34/5/002 **34**(5), 573– 587 (1989).

10 N. J. Pelc, "*A generalized filtered backprojection algorithm for three dimensional reconstruction*," PhD thesis, Harvard University, 1979.

11 J. D. O'sullivan, " A fast sinc function gridding algorithm for Fourier inversion in computer tomography," *IEEE Trans. Med. Imaging* **4**(4), 200– 207 (1985).

12 J. I. Jackson, C. H. Meyer, D. G. Nishimura, and A. Macovski, " Selection of a convolution function for Fourier inversion using gridding," *IEEE Trans. Med. Imaging* 10.1109/42.97598 **10**, 473– 478 (1991).

13 C. H. Meyer, B. S. Hu, D. G. Nishimura, and A. Macovski, " Fast spiral coronary artery imaging," *Magn. Reson. Med.* **28**, 202– 213 (1992).

14 J. G. Pipe and P. Menon, " Sampling density compensation in MRI: Rationale and an iterative numerical solution," *Magn. Reson. Med.* 10.1002/(SICI)1522-2594(199901)41:1<179::AID-MRM25>3.0.CO;2-V **41**, 179– 186 (1999).

15 V. Rasche, R. Proska, R. Sinkus, P. Bornert, and H. Eggers, " Resampling of data between arbitrary grids using convolution interpolation," *IEEE Trans. Med. Imaging* 10.1109/42.774166 **18**(5), 385– 392 (1999).

16 H. Sedarat and D. G. Nishimura, " On the optimality of the gridding reconstruction algorithm," *IEEE Trans. Med. Imaging* **19** (4), 306– 317 (2000).

17 D. Rosenfeld, " An optimal and efficient new gridding algorithm using singular value decomposition," *Magn. Reson. Med.* **40**, 14– 23 (1998).

18 D. Rosenfeld, " New approach to gridding using regularization and estimation theory," *Magn. Reson. Med.* **48**, 193– 202 (2002).

19 G. Besson, " CT image reconstruction from fan-parallel data," *Med. Phys.* 10.1118/1.598533 **26**(3), 415– 426 (1999).

20 C. R. Crawford, " CT filtration aliasing artifacts," *IEEE Trans. Med. Imaging* **10**(1), 99– 102 (1991).

21 C. W. Stearns, C. R. Crawford, and H. Hu, " Oversampled filters for quantitative volumetric PET reconstruction," *Phys. Med. Biol.* **39**, 381– 387 (1994).

22 P. E. Kinahan and J. G. Rogers, " Analytic 3D image reconstruction using all detected events," *IEEE Trans. Nucl. Sci.* 10.1109/23.34585 **36**(1), 964– 968 (1989).
23 D. A. Chesler, S. J. Riederer, and N. J. Pelc, " Noise due to photon counting statistics in computed x-ray tomography," *J. Comput. Assist. Tomogr.* **1**, 64– 74 (1977).
24 E. G. Solomon, B. P. Wilfley, M. S. Van Lysel, A. W. Joseph, and J. A. Heanue, " *Scanning-beam digital x-ray (SBDX) system for cardiac angiography*," in *Medical Imaging 1999: Physics of Medical Imaging*, Vol. **3659** (SPIE, Bellingham, WA, 1999), pp. 246– 257.
25 M. E. Daube-Witherspoon and G. Muehllehner, " Treatment of axial data in three-dimensional PET," *J. Nucl. Med.* **36**, 1717– 1724 (1987).
26 M. Defrise, P. E. Kinahan, D. W. Townsend, C. Michel, M. Sibomana, and D. F. Newport, " Exact and approximate rebinning algorithms for 3-D PET data," *IEEE Trans. Med. Imaging* 10.1109/42.563660 **16** (2), 145– 158 (1997).
27 M. Defrise and X. Liu, " A fast rebinning algorithm for 3D positron emission tomography using john's equation," *Inverse Probl.* **15**(4), 1047– 1065 (1999).
28 S. Matej, J. S. Karp, R. M. Lewitt, and A. J. Becher, " Performance of the Fourier rebinning algorithm for PET with large acceptance angles," *Phys. Med. Biol.* **43**(5), 573– 587 (1998).
29 A. J. Reader, D. Visvikis, K. Erlandsson, R. J. Ott, and M. A. Flower, " Intercomparison of four reconstruction techniques for positron volume imaging with rotating planar detectors," *Phys. Med. Biol.* **43**(4), 823– 834 (1998).
30 M. L. Egger and C. Morel, " Execution times of five reconstruction algorithms in 3D positron emission tomography," *Phys. Med. Biol.* 10.1088/0031-9155/43/3/020 **43**(3), 703– 712 (1998).
31 T. H. Farquhar, A. Chatziioannou, and S. R. Cherry, " An evaluation of exact and approximate 3-D reconstruction algorithms for a high-resolution, small-animal PET scanner," *IEEE Trans. Med. Imaging* **17**(6), 1073– 1080 (1998).